

Cross-Barrier Flow during Orographic Precipitation Events: Results from MAP and IMPROVE

SOCORRO MEDINA, BRADLEY F. SMULL, AND ROBERT A. HOUZE JR.

Department of Atmospheric Sciences, University of Washington, Seattle, Washington

MATTHIAS STEINER

Department of Civil and Environmental Engineering, Princeton University, Princeton, New Jersey

(Manuscript received 20 February 2004, in final form 1 February 2005)

ABSTRACT

Ground-based and airborne Doppler radar data collected during passage of frontal rainstorms over the European Alps and Cascade Mountains of Oregon are found to exhibit characteristic cross-barrier flow and precipitation patterns. A stably stratified layer of blocked (or partially blocked) low-momentum flow below mountain-crest level is separated from strong cross-barrier flow aloft by a concentrated layer of vertical wind shear. This shear layer slopes upward toward the mountain crest and persists for several hours as the storm passes over the mountain range. This pattern is remarkably similar from case to case and from one mountain range to the other. The orographically enhanced precipitation in these cases exhibits stratiform structure, marked by a radar bright band, which often drops to a lower height (indicating locally cooler conditions) immediately adjacent to the windward mountain slopes. A terrain-induced gravity wave produces strong downslope flow and spillover of precipitation onto the lee side of the barrier. An elevated reflectivity maximum appears above the mountain crest and extends a short distance (generally 20–40 km) upstream, apparently as a result of gravity wave lifting. While baroclinically induced shear may contribute to the observed pattern, two-dimensional idealized simulations indicate that, in the presence of sufficient upstream static stability, orographic effects alone are sufficient to support development of the upward-sloping shear layer on the windward side of the barrier. Furthermore, idealized simulations show that if there is preexisting vertical shear in the incident upstream flow, this shear is strengthened by the orography and that surface friction may also enhance the strength of the shear layer.

The repeatable sheared velocity pattern identified here is apparently an essential feature of cases in which stably stratified low-level flow associated with a baroclinic system impinges upon a sufficiently tall mountain range. Since the layer of orographically generated shear promotes turbulence, which has been shown to aid precipitation growth over the windward slopes, these stable flow dynamics represent a potentially important mechanism for orographic precipitation enhancement in association with the passage of frontal systems over mountainous terrain.

1. Introduction

The interaction of moist flow with underlying mountainous terrain depends on multiple factors. These include the static stability, moisture content, strength of the cross-barrier wind, and shear profile of the incident upstream flow, as well as the configuration of the topography. The myriad of possible combinations of

these factors requires studies to limit themselves to a finite range of conditions. This study concentrates upon moist, statically stable flows associated with baroclinic precipitation systems approaching major mountain ranges. We seek to identify those mechanisms leading to repeatable aspects of the response of the flow and precipitation to the underlying steep terrain.

Pierrehumbert and Wyman (1985) found that flow impinging on a mountain range may sharply differ in zones above and below mountain-top level. During several Alpine Experiment (ALPEX) cases observed under various synoptic conditions, the airflow below the crest was to some degree diverted around the Alps,

Corresponding author address: S. Medina, Box 351640, Dept. of Atmospheric Sciences, University of Washington, Seattle, WA 98195-1640.

E-mail: socorro@atmos.washington.edu

whereas the airflow above crest level crossed the barrier with little evidence of orographic perturbation in the upstream region. From analyses of statically stable storms over the Sierra Nevada, Marwitz (1987) found that the cross-barrier winds were at times profoundly blocked at low levels, however they increased very rapidly with height, exceeding 20 m s^{-1} over the crest. Details of this flow structure and its relationship to the orography and ensuing precipitation pattern were limited, however, by the mode of data collection possible at that time. Recent studies over widely different geographic locations have documented storms with cross-barrier flow bearing some similarities to that observed by Marwitz (1987) [e.g. over the Olympic Mountains in western Washington and Vancouver Island (Colle and Mass 1996) and over the Wasatch Range of Utah (Cox et al. 2002)]. The Mesoscale Alpine Program (MAP; Bougeault et al. 2001), conducted over the European Alps in September–November 1999, brought to bear a wide variety of sophisticated aircraft and ground-based observational platforms to examine orographically modified flow in much greater detail. For example, for a case of strong upstream blocking during 21 October 1999 [intensive observing period (IOP)8], Medina and Houze (2003) showed that low-level flow adjacent to the south-facing slopes of the Alps surrounding the Lago Maggiore region was approximately parallel to the topography, whereas at higher levels, winds veered to become cross barrier. In this same storm, Bousquet and Smull (2003b) observed profoundly blocked flow at low-levels and sloped cross-barrier flow toward the southern (windward) side of the Alps at higher altitudes.

These previous analyses of stable orographic storms over different geographic regions and synoptic conditions suggest that airflow patterns on the windward slope of the terrain may exhibit certain key similarities, which in turn indicate that recurring dynamical mechanisms and associated precipitation processes are at work. The objective of this paper is to document in unprecedented detail the repeatability of cross-barrier flow patterns on the windward slopes of major mountain barriers during statically stable orographic precipitation events and to explore the role of steep terrain in their development. Houze and Medina (2005) found that a shear layer separating low-level blocked or partially blocked flow from upper-level unblocked flow appears to play an important role in the precipitation enhancement process over the windward slopes. This paper examines how this shear layer develops as a baroclinic system passes over the mountain barrier. The study uses datasets collected over the European Alps during MAP (September–November 1999) and over

the Oregon Cascade Range during the second Improvement of Microphysical Parameterization through Observational Verification Experiment (IMPROVE-2, November–December 2001; Stoelinga et al. 2003). Similar instrumentation was deployed in each of these projects to observe orographic precipitation processes. MAP and IMPROVE-2 therefore constitute highly analogous datasets suitable for investigating the repeatability of the terrain-modified airflow in diverse geographical locations. Two-dimensional (2D) numerical simulations conducted with the Weather Research and Forecasting (WRF) model allow us to further interpret and extend these new observational results.

2. Data

The experimental area for MAP was the Lago Maggiore region, which is partially encircled by the Mediterranean-facing slopes of the Alps (Fig. 1a). The Alps have a crest line reaching $\sim 4 \text{ km}$ [unless otherwise stated, all altitudes are above mean sea level (MSL)]. The IMPROVE-2 experimental area was located to the west of the Oregon Cascade Mountains, which exhibit a crest near $\sim 2 \text{ km}$ (Fig. 1b). The National Center for Atmospheric Research (NCAR) S-band dual-polarization radar (S-Pol) provided continuous radial velocity, reflectivity and hydrometeor type information in both domains (Fig. 1). The S-Pol radar specifications and scanning strategies are described in Medina and Houze (2003) for MAP and in Houze and Medina (2005) for IMPROVE-2. The National Oceanic and Atmospheric Administration (NOAA) WP-3D (P-3) aircraft equipped with a fore–aft-scanning X-band tail-mounted Doppler radar provided detailed vector airflow information at key times and at locations obscured from the view of the ground-based radar. The analysis technique applied to the P-3 airborne radar observations to obtain three-dimensional (3D) airflow and precipitation structures is described by Bousquet and Smull (2003a,b).

Upstream sounding data in MAP were obtained at Milan (Fig. 1a). In IMPROVE-2, soundings were obtained by a mobile University of Washington (UW) sonde unit (Fig. 1b). Infrared satellite images and synoptic fields from numerical models are used to place the radar data into a large-scale context. For MAP, numerical weather prediction model output generated by the European Centre for Medium-Range Weather Forecasts (ECMWF) is used. For IMPROVE-2, output from the UW operational fifth-generation Pennsylvania State University (PSU)–NCAR Mesoscale Model (MM5) is used. Idealized simulations constructed using

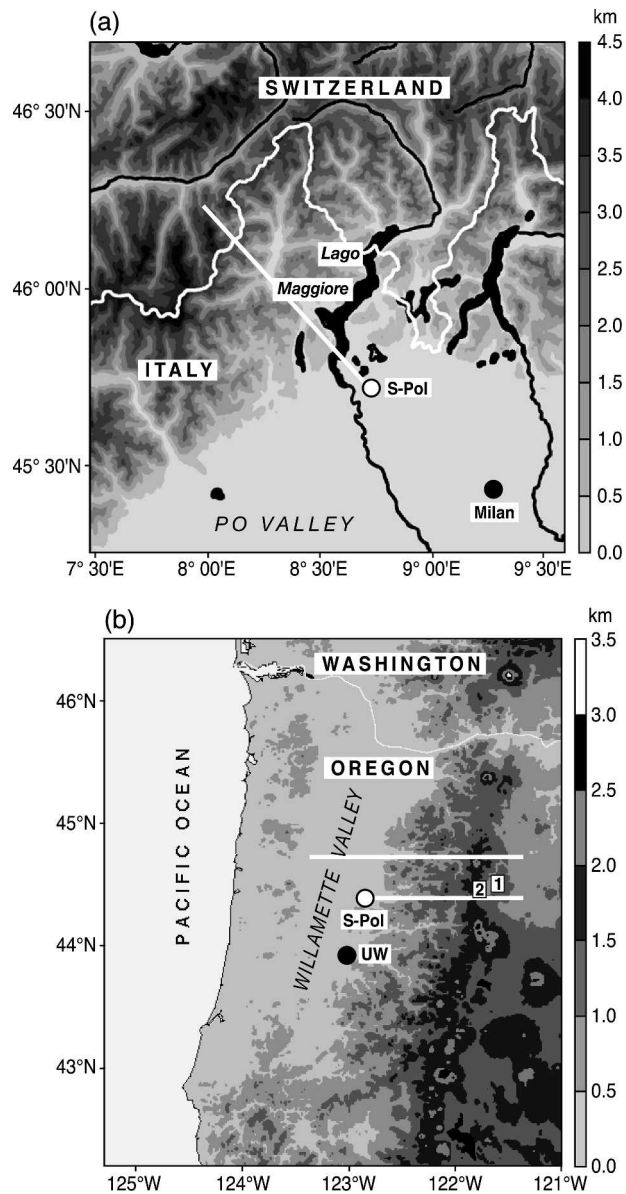


FIG. 1. Observational areas for (a) MAP and (b) IMPROVE-2, showing the location of the S-Pol radar (white dot), upper-air sounding site (black dot), and the location of vertical cross sections (white lines) discussed in the text in relation to topography (shaded terrain height according to key). In (b) 1 and 2 mark the locations of Camp Sherman and Corbett Sno-Park, respectively.

the WRF model (Michalakes et al. 2001; Skamarock et al. 2001) are also presented. The important parameters used to create these simulations are described in section 5a.

3. Synoptic conditions

In this study, data from three exceptionally well-observed storms will be presented: one case from MAP

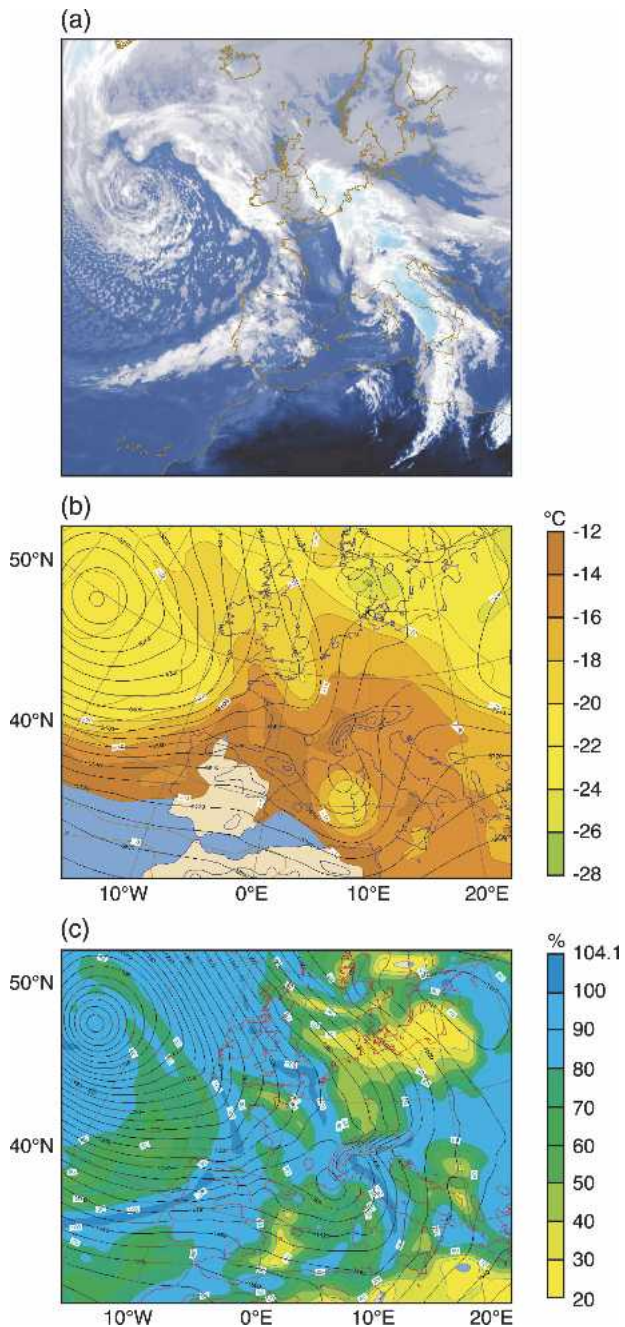


FIG. 2. (a) Infrared satellite image at 1200 UTC 21 Oct 1999, (b) 500-mb geopotential height (black contours, 40-m interval) and air temperature ($^{\circ}\text{C}$, color shading), and (c) 850-mb geopotential height (black contours, 20-m interval) and relative humidity (% , color shading) from 12-h ECMWF forecast valid at 1200 UTC 21 Oct 1999.

(Fig. 2), and two from IMPROVE-2 (Figs. 3 and 4). On 21 October 1999 (MAP IOP8), a frontal system (Fig. 2a) and associated baroclinic trough (Fig. 2b) approached the Alps. Strong southerly flow was observed

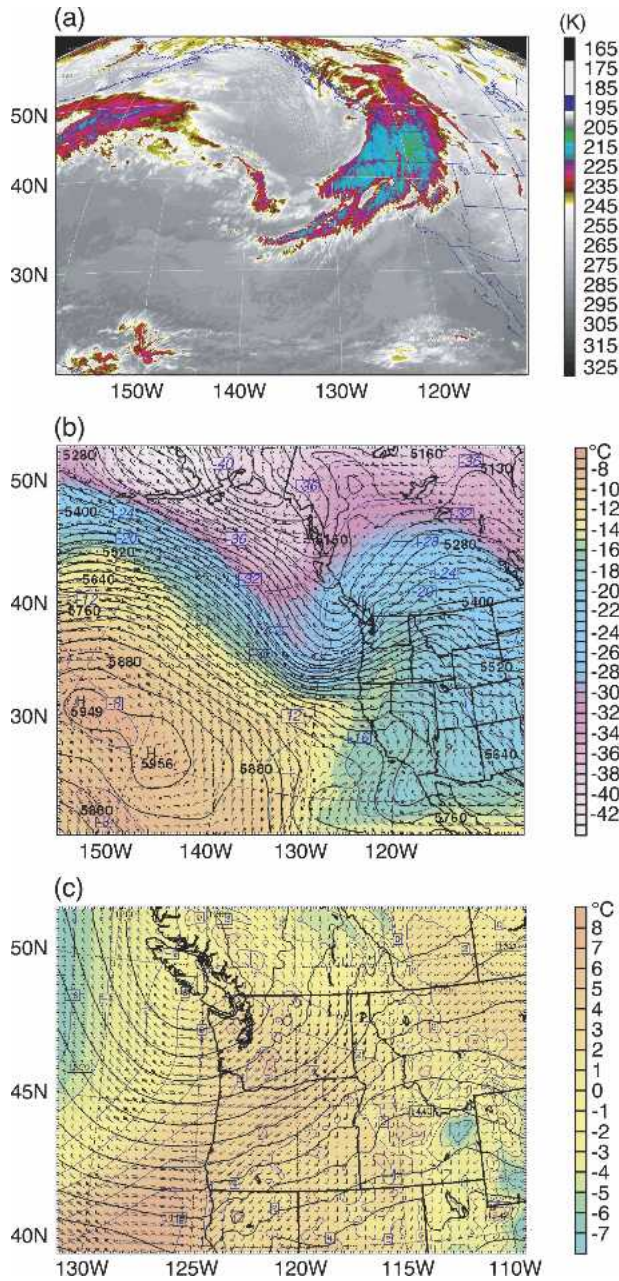


FIG. 3. (a) Infrared satellite image at 0000 UTC 14 Dec 2001, (b) MM5 500-mb geopotential height (black contours, 30-m interval), air temperature (color shading) and wind field from initialized UW operational 36-km run, and (c) MM5 850-mb geopotential height (black contours, 30-m interval), air temperature (color shading), and winds from initialized UW operational 12-km resolution run valid at 0000 UTC 14 Dec 2001.

at 850 mb over the Ligurian Sea, upstream of the Alps and the Apennines (Fig. 2c). Various aspects of the low-level flow observed during this case have been documented by Bousquet and Smull (2003a,b), Medina and Houze (2003), Rotunno and Ferretti (2003), and

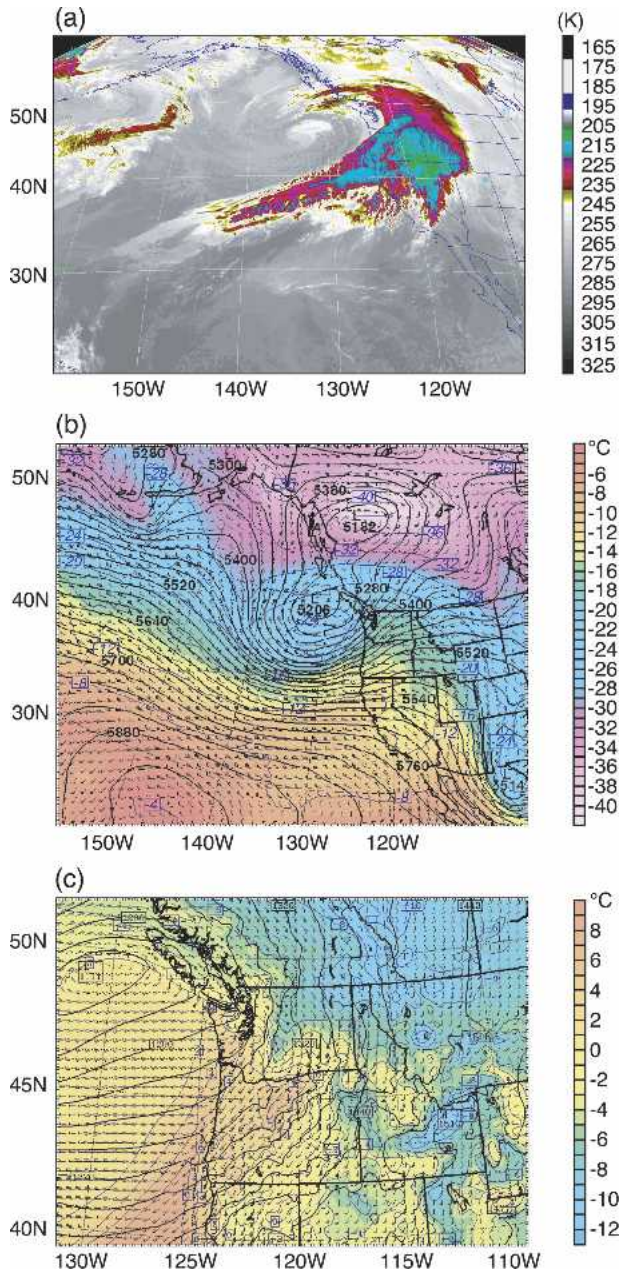


FIG. 4. (a) Infrared satellite image at 1700 UTC 28 Nov 2001, (b) MM5 500-mb geopotential height (black contours, 30-m interval), air temperature (color shading), and wind field from 6-h forecast UW operational 36-km run, and (c) MM5 850-mb geopotential height (black contours, 30-m interval), air temperature (color shading), and winds from 6-h forecast UW operational 12-km run valid at 1800 UTC 28 Nov 2001.

Steiner et al. (2003), among others. According to an upstream sounding taken at Milan (Fig. 1a) at 0600 UTC 21 October, the squared dry (N_d^2) and moist (N_m^2) Brunt-Väisälä frequencies [the latter being calculated following Durran and Klemp (1982)] were both posi-

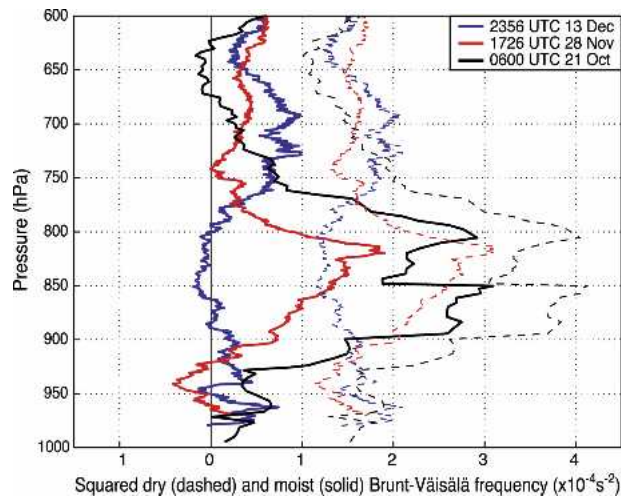


FIG. 5. Vertical profiles of squared Brunt-Väisälä frequency calculated using the Milan sounding (Fig. 1a) collected at 0600 UTC 21 Oct 1999 (black line), and the UW mobile sonde unit (Fig. 1b) collected at 2356 UTC 13 Dec 2001 (blue line) and at 1726 UTC 28 Nov 2001 (red line).

tive, indicating an absolutely stable stratification (Fig. 5, black lines).

A particularly intense and well-defined frontal system (Fig. 3a) and upper-level trough (Fig. 3b) passed over the Pacific Northwest and IMPROVE-2 experimental domain on 13–14 December 2001. As a result, westerly winds were observed at 850 mb over the Oregon coast (Fig. 3c). A detailed synoptic and mesoscale description of this case using observations and MM5 output is given by Garvert et al. (2005). The observed microphysical characteristics of this storm are described by Houze and Medina (2005) and Woods et al. (2005). An upstream sounding taken at 2356 UTC 13 December 2001 showed statically stable flow everywhere, except for a neutral layer between 800 and 850 mb for saturated flow (Fig. 5, blue lines). A similar but somewhat less intense storm passed over the IMPROVE-2 network on 28 November 2001. The synoptic conditions off the Oregon coast (Fig. 4) and upstream stability of air approaching the Cascade Range (Fig. 5, red lines) generally resembled those for the 13–14 December case.

Each of these three events thus embodied a baroclinic system impinging upon an orographic barrier. In each case, the upstream flow was generally stable and the wind direction at 850 mb was quasi perpendicular to the mountain range. As these systems passed over the respective mountain ranges, the cross-barrier flow and precipitation patterns were modified in a similar way. The next section describes these associated characteristics in detail.

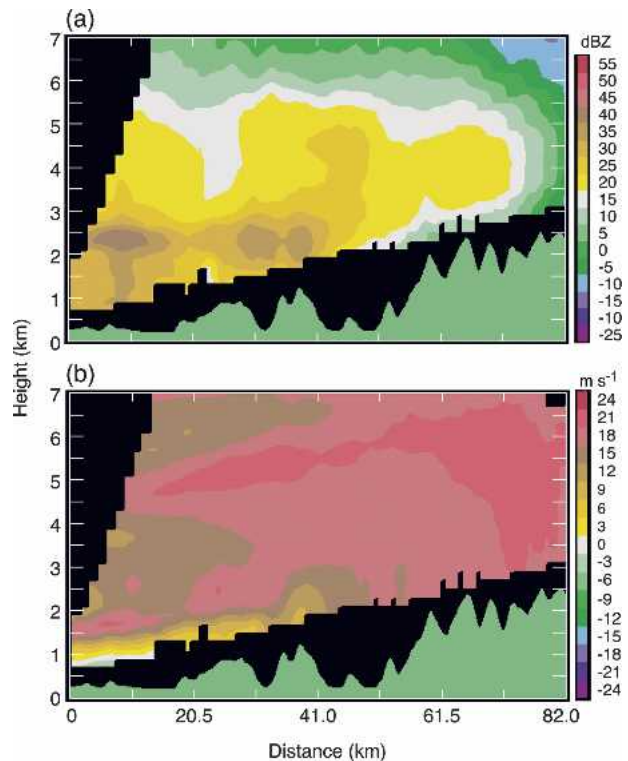


FIG. 6. Vertical cross section of S-Pol radar data extending from the radar site, located at the lower-left corner of each panel, extending northwest across the Alps (along the white line in Fig. 1a). (a) Reflectivity (dBZ) and (b) radial velocity (m s^{-1}) at 0957 UTC 21 Oct 1999. In (b) positive values denote flow away from the radar (i.e., from left to right). Topography (green shading) is shown in the lower part of each panel.

4. Observed cross-barrier flow and precipitation in cases with stable stratification

a. Alpine storm (MAP IOP8)

Figure 6 shows a vertical cross section of S-Pol radar data collected at 0957 UTC 21 October 1999, during MAP IOP8. This section extends from the S-Pol radar (on the left in Fig. 6) across the Alps to the northwest, that is, in a direction approximately perpendicular to the local topography (cf. white line marking this section's location in Fig. 1a). The reflectivity pattern exhibited a bright band at ~ 2.3 km, characterizing the precipitation as stratiform (Fig. 6a). Figure 6b shows the corresponding radial velocity field with green and blue (yellow and red) shading denoting flow toward (away from) the radar. The white contour denotes radial velocities $\sim 0 \text{ m s}^{-1}$. At ranges close to the radar near 1.0-km altitude lies the highly sheared layer ($\sim 18 \text{ m s}^{-1} \text{ km}^{-1}$). This layer sloped upward with distance toward the Alpine crest, and exhibited a pronounced upward perturbation in the vicinity of a localized peak

in the foothills (immediately left of the 41.0-km range mark in Fig. 6b). Above this layer, flow was strong and directed away from the radar, that is, climbing the terrain in a cross-barrier direction, while the radial component of the flow at lower levels was weak and directed toward the radar (i.e., away from the higher terrain). The highly sheared nature of the flow persisted for several hours, as indicated by a 3-h mean of radial velocity (Fig. 20 in Houze and Medina 2005). The NOAA P-3 aircraft collected nearly contemporaneous radar data within the cross section shown in Fig. 6. Figure 7a shows the reflectivity and flow component in the plane of the cross section (Fig. 7b) as derived from airborne Doppler radar data. The reflectivity exhibited a clearly defined bright band (Fig. 7a). In Fig. 7a, peak reflectivities defining the bright band fell to a lower height immediately adjacent to the steeply rising Alpine terrain, consistent with other evidence of locally cooler air at the foot of the Alps as shown by Bousquet and Smull (2003b; see especially their Figs. 2 and 3). Marwitz (1983, 1987) noted a similar dip in the 0°C isotherm close to the windward slopes of the Sierra Nevada, and suggested that this effect was associated with increased melting and diabatic cooling resulting from high precipitation rates over the windward slope. Another possibility, suggested by Bousquet and Smull (2003b) in the context of MAP IOP8, is that the pre-existing cool air present over the Po Valley was eroded from the south, leaving lower temperatures to the north, as indicated by Fig. 7a. To the degree that stably stratified air at the top of the shear layer was locally forced to gently ascend the barrier (as suggested by upward sloping contours of positive cross-barrier flow below/through the brightband layer), adiabatic ascent may further contribute to this cooling, as described by Mass and Ferber (1990).

Airborne radar provided information in some regions that were obscured from the view of the ground-based radar. When compared to the radial velocity from the ground-based radar (Fig. 6b), the airborne-Doppler-derived flow component in the plane of the cross section (Fig. 7b) shows reasonable agreement in regions of overlap. The full extent of the shear layer is not evident from the ground-based radar because of blockage of the beam by the terrain and decreased resolution (i.e., beam broadening) at more distant ranges. The airborne radar view shows that the shear layer was not only present over the lower Alpine slopes, but also extended over the higher terrain (cf. Figs. 7b and 6b). The ground-based radar could not observe low-level conditions beyond intervening peaks within the Alpine foothills, however airborne radar data clearly show weak and reversed (downslope) flow

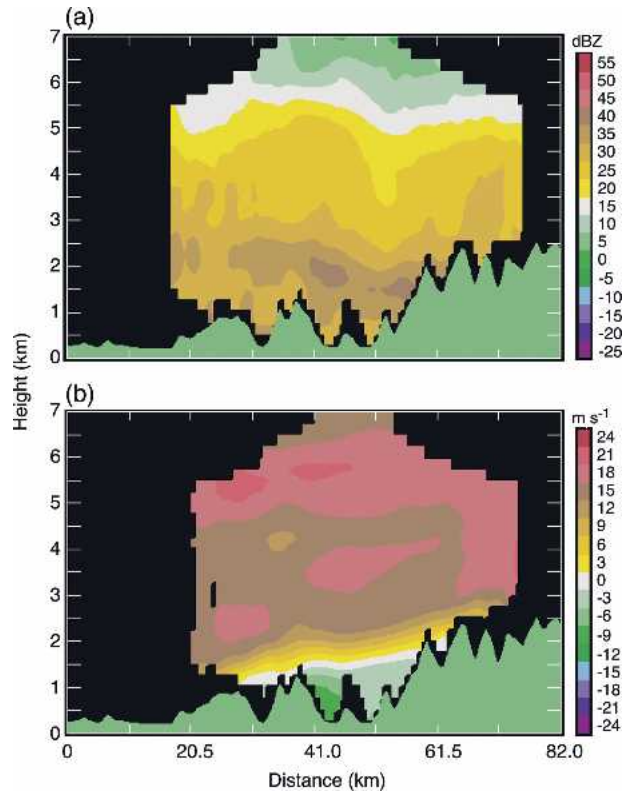


FIG. 7. Vertical cross section of P-3 airborne radar analyses of (a) reflectivity (dBZ) and (b) airflow in the direction of the cross section (m s^{-1}) based on data collected around 0952 UTC 21 Oct 1999. In (b) positive values denote flow from left to right. Cross-section location is identical to that shown in Fig. 6. Topography (green shading) is shown in the lower part of each panel.

within these deep valleys (Fig. 7b), which in turn contributed to blocked flow farther upstream of the range, as pointed out by Steiner et al. (2003) and Bousquet and Smull (2003b).

b. Oregon Cascades storm (IMPROVE-2 13–14 December 2001 case)

Figure 8 shows a vertical cross section of S-Pol radar data collected at 2343 UTC 13 December 2001 during an IMPROVE-2 case in which widespread heavy rainfall accumulations occurred. These data were quality controlled close to the terrain to remove ground clutter (Houze and Medina 2005). The cross sections extend from the S-Pol radar (on the left in Fig. 8) across the Oregon Cascade Range to the east, in a direction perpendicular to the topography (cf. section location shown by southernmost white line in Fig. 1b). The reflectivity had a stratiform structure characterized by a bright band at ~ 1.8 km that sloped slightly downward adjacent to the higher terrain, and a secondary maximum at ~ 3.0 – 5.0 km altitude and ~ 55 km range from

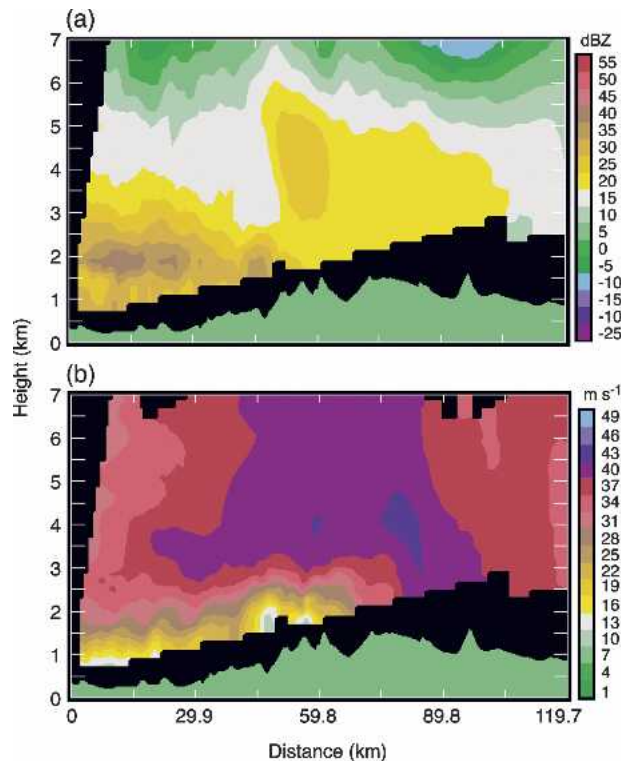


FIG. 8. Vertical cross section of S-Pol data extending from the radar site, located at the lower-left corner of each panel, extending eastward across the Cascades (along the southernmost white line in Fig. 1b). (a) Reflectivity (dBZ) and (b) radial velocity (m s^{-1}) at 2343 UTC 13 Dec 2001. In (b) positive values denote flow away from the radar (i.e., from left to right). Topography (green shading) is shown in the lower part of each panel.

the radar (Fig. 8a). All the radial velocities values in Fig. 8b are positive, that is, corresponding to flow directed away from the radar, thus indicating flow toward the barrier at all levels. At the lowest level where data were available, the radial flow speed was 10 m s^{-1} . However, airborne radar data, available very close to the surface, measured cross-barrier flow as low as $\sim 4 \text{ m s}^{-1}$ (Fig. 9b). At 850 mb, the UW 12-km MM5 operational simulation (Fig. 3c) shows downgradient flow immediately upstream of the Cascade Range, indicative of subgeostrophic cross-barrier flow in this zone of partial blocking. Over the Willamette Valley (Fig. 1b), the cross-barrier (U) and along-barrier (V) components of the flow at 850 mb were ~ 23 and 17 m s^{-1} , respectively. By way of comparison, the cross- and along-barrier geostrophic values (determined by analyzing the meridional and zonal geopotential height gradients in Fig. 3c) were $U_g \sim 36 \text{ m s}^{-1}$ and $V_g \sim 7 \text{ m s}^{-1}$, respectively. Therefore $U < U_g$ and $V > V_g$, illustrating the degree to which the winds were affected by the presence of the barrier (Marwitz 1987).

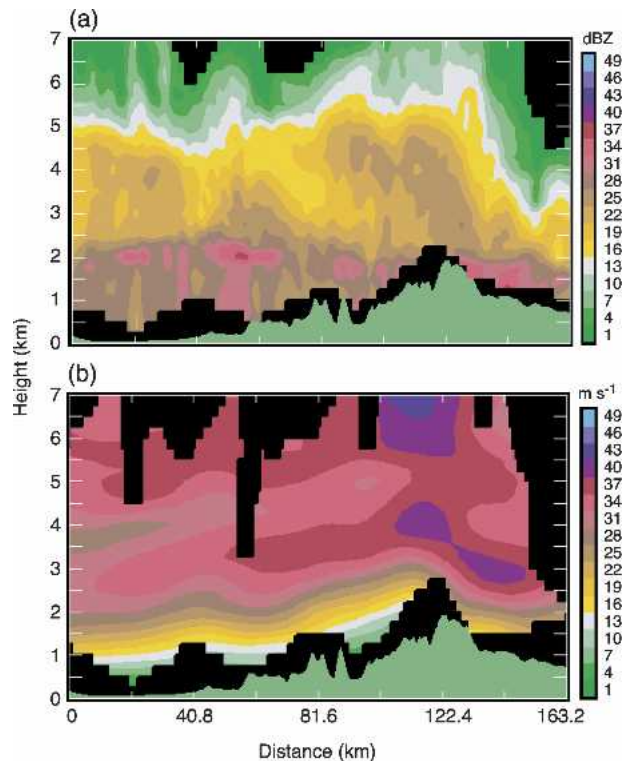


FIG. 9. Vertical cross section of P-3 airborne radar analyses extending west–east from the Willamette Valley across the Cascade crest (along the northernmost white line in Fig. 1b). (a) Reflectivity (dBZ) and (b) airflow in the direction parallel to the cross section (m s^{-1}) based on data collected over a ~ 45 min period centered at 0000 UTC 14 Dec 2001. In (b) positive values denote flow from left to right. Topography (green shading) is shown in the lower part of each panel.

The low-level flow was directed toward the terrain at all levels during the IMPROVE-2 13–14 December case, as opposed to the more profound blocking (downslope low-level flow) observed during MAP IOP8, although this flow was significantly retarded by the terrain. Several factors likely contributed to the reversal of low-level flow during MAP IOP8: exceptionally strong stability, the presence of a preexisting cool air mass over the Po Valley, and the sharply ascending Alpine topography. Compared to IOP8, the 13–14 December IMPROVE-2 case was less stable (Fig. 5) and possessed stronger crest-level winds (cf. Figs. 6b and 8b) surmounting a somewhat lower barrier—a configuration that evidently was not conducive to the formation of fully blocked flow.

During the 13–14 December case, weak flow at low levels was again bounded above by a layer of substantial shear separating it from the strong cross-barrier flow aloft (Fig. 8b). The shear layer is seen to extend almost to the crest of the mountain range, even subject

to the limitations of the ground-based radar discussed in section 4a. These characteristic patterns of flow and precipitation persisted for several hours, and are thus also clearly evinced in 3-h averages of reflectivity and radial velocity (Fig. 8 in Houze and Medina 2005).

The NOAA P-3 aircraft mapped widespread reflectivity and flow patterns encompassing the region shown in Fig. 8, but unfortunately a brief malfunction of the airborne radar prevented sampling along this particular section. Figure 9 thus shows P-3 reflectivity and cross-barrier flow patterns along an analogous west–east section located ~ 40 km north of that shown in Fig. 8 (northernmost white line in Fig. 1b). To span a broad cross-barrier distance, this display was constructed from a composite of airborne radar data collected over a ~ 45 min period centered at 0000 UTC 14 December. Although the times and locations of data shown in Figs. 8 and 9 are somewhat different, the general features depicted are quite similar. Examination of many such sections within the airborne Doppler analysis domain indicates that these flow and precipitation features were ubiquitous along this relatively 2D segment of the Cascade Range. The reach of airborne radar coverage into the leeside region captures downward-sloping flow contours consistent with the presence of a terrain-induced gravity wave (Fig. 9b). Further evidence of strong downslope winds consistent with a well-developed mountain wave over central Oregon was provided by reports of damaging winds during this period (National Climatic Data Center 2001). In conjunction with ice particle collection work performed near Santiam Pass during IMPROVE-2, M. Garvert (2004, personal communication) experienced strong winds and witnessed significant tree damage between Camp Sherman and Corbett Sno-Park (locations marked 1 and 2 in Fig. 1b, respectively) in central Oregon around 2300 UTC 13 December 2001.

The reflectivity pattern measured by the airborne radar exhibits a bright band whose height varies in the horizontal, but once again tends to dip downward adjacent to the windward- (west) facing slopes of the higher terrain (Fig. 9a), in a manner similar to that seen in Fig. 8a and to that observed during MAP IOP8 (cf. Fig. 7a). Both diabatic (Marwitz 1983, 1987) and adiabatic effects may contribute to localized cooling. Surface pressure patterns derived from the UW 12-km MM5 operational run (not shown) depict a characteristic upstream-ridging/lee-troughing pressure perturbation couplet of the sort identified by Mass and Ferber (1990). The reflectivity showed an elevated (3.5–5-km altitude) secondary maximum at 90–120-km ranges and spillover of precipitation into the lee of the Cascades (cf. plume of values >25 dBZ in Fig. 9a) as a result of

hydrometeors being transported to lower levels by the downslope flow associated with the gravity wave (Colle 2004).

Jiang (2003, see his Fig. 1) used a mesoscale model to simulate stable ascent of orographic precipitation over a Gaussian-shaped mountain of maximum height $h = 1.0$ km. In his simulations, precipitation forms on the windward slope, as expected from the forced ascent, and also over the lee side of the mountain as a result of gravity wave lifting. This area of simulated precipitation is located at low levels on the lee side and shows an upstream tilt with height. In Jiang's model, the precipitation associated with the gravity wave response extends to elevations as high as 5 km over the mountain crest, consistent with the observed development of an elevated secondary maximum in reflectivity documented in Figs. 8a and 9a. Using a 2D mesoscale simulation over a mountain barrier having height and width characteristics similar to the Cascade Range, Colle (2004) showed that a terrain-induced gravity wave can develop for incident wind speeds >20 m s $^{-1}$, producing a layer of upward motion that extends to the windward side. The shape and distribution of precipitation in relation to the mountain crest of Colle's orographic response (indicated by snow mixing ratio contours) was similar to the observed secondary maximum of reflectivity, further suggesting that this maximum could be associated with a terrain-induced gravity wave.

c. Oregon Cascades storm (IMPROVE-2 28 November 2001 case)

Figure 10 shows a vertical cross section of S-Pol radar data collected from 1600 to 1900 UTC 28 November, during the earliest days of IMPROVE-2. The location of this cross section relative to the terrain is identical to that in Fig. 8. The flow direction was everywhere away from the radar, indicating upslope cross-barrier flow (Fig. 10b). The mean radial velocity again exhibited a sheared layer sloping upward over the terrain, similar to the structure observed during MAP IOP8 and during 13–14 December 2001 (Figs. 6b and 8b). There were no airborne Doppler radar data collected for this case, however, the available ground-based measurements exhibit strong similarity to those cases previously discussed, including evidence of an upward-sloping layer of strong shear and localized deepening of the low-level retarded flow (as indicated by an upward bulge of the velocity contours near the zone of most sharply rising terrain).

The time–mean reflectivity pattern was again of a profoundly stratiform nature, exhibiting a bright band centered near ~ 2.3 km that sloped downward and deepened immediately adjacent to the sharply rising

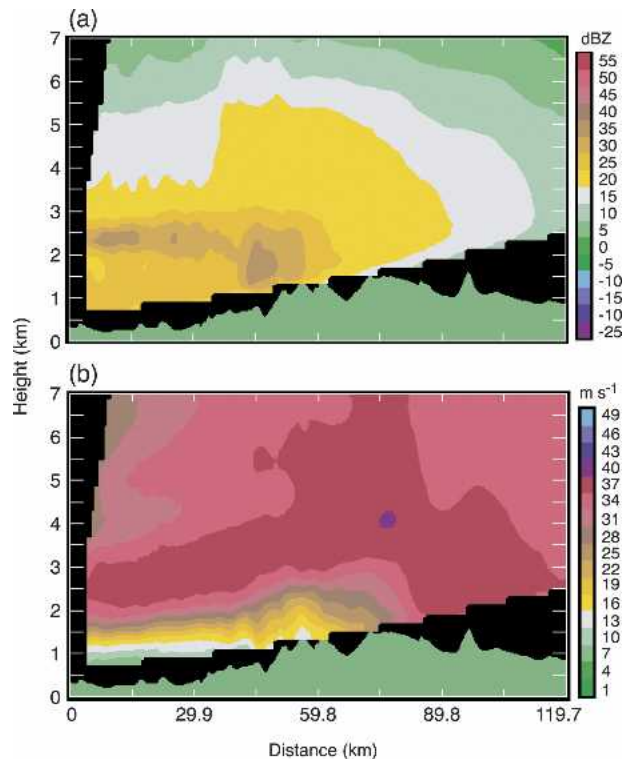


FIG. 10. As in Fig. 8, except for showing fields averaged over the interval 1600–1900 UTC 28 Nov 2001.

terrain. An elevated layer of enhanced reflectivities was again detected at altitudes of 4.0–5.5 km for ranges >35 km (Fig. 10a). This precipitation enhancement signature appeared in concert with a zone of increased westerly, that is, (positive/outbound radial flow) marking the upstream edge of a mountain wave signature. The envelope of accelerated westerly flow extended downward beyond the Cascade crest, where rapidly decreasing reflectivity values indicate rapid evaporation (sublimation) of precipitation in association with strong lee-side subsidence.

d. Discussion

Based upon this expanded body of observations, we may speculate on variety of mechanisms that might contribute to the existence and/or maintenance of stably stratified airflow and associated shear impinging upon major mountain barriers, which in turn have the potential to significantly impact orographic precipitation processes. In the Cascade region of the Pacific Northwest, prior transit of landfalling storms and their attendant air masses over the cool yet relatively temperate waters of the Pacific undoubtedly plays an important role in determining the low-level stratification. In other situations, such as some cases observed over

the more continental regime of the European Alps, prior incursions of less-modified polar air masses may initiate stable conditions, but these may once again interact with moist cross-barrier flows generated by transitory baroclinic disturbances. The mechanisms involved in the maintenance of such stable stratification in the face of persistent cross-barrier advection have yet to be described, but are likely sensitive to the precipitation processes themselves (e.g., the role of evaporation- and melting-induced cooling rates), thus representing a potentially important and highly nonlinear feedback mechanism. Neither can the potential influence of surface friction or other sources of turbulent dissipation be ignored, particularly over regions of complex terrain.

Precipitation patterns accompanying these strongly sheared flows routinely evince stratiform structure, including a pronounced radar bright band in the observed reflectivity pattern. For the cases documented herein, the bright band frequently drops to a lower height and/or deepens immediately adjacent to the steepest mountain slopes (cf. Figs. 7a, 8a, and 9a), as was previously noted by Bousquet and Smull (2003b, see their Fig. 8a and related discussion). Marwitz (1983, 1987) directly observed a local negative temperature perturbation immediately above the steep windward slope of the Sierras, and speculated on its relationship to increased precipitation rates and cooling through diabatic effects.

More generally, Houze and Medina (2005) found that the horizontally expansive shear layer has the potential to promote small-scale updraft cells that foster riming and aggregation. Melting of larger (e.g., rimed) particles could conceivably lead to diabatic cooling rates extending through a deeper layer, thus representing a localized stabilizing influence (as suggested by observed flow perturbations in this zone). Adiabatic effects may also be important as the flow atop the shear layer is rapidly forced to ascend the barrier. In any case, such localized cooling may provide a positive feedback by reinforcing the shear layer. If this feedback is important in creating or modulating the strength of the shear layer, it would depend critically upon the intersection of the 0°C level with the effective topography in order for this mode of precipitation enhancement to occur, as was previously suggested by Meyers and Cotton (1992).

Further coordinated measurements of thermal stratification, airflow and precipitation processes are needed to confirm and quantify such microphysical feedbacks, if they indeed exist. The hypotheses posed in this study thus require detailed temperature profiles at various distances from the crest as well as airflow data to be fully tested by observational means. In lieu of such

measurements, we turn to a suite of idealized simulations to explore the dependence of cross-barrier flow patterns (and in particular, development of enhanced vertical shear) upon the aspects of larger-scale atmospheric conditions and underlying terrain structures that routinely support development of significant orographic precipitation.

5. Idealized simulations

a. Model description and experimental approach

To gain further insight into the mechanisms responsible for producing the characteristic cross-barrier flow patterns described in section 4, and to investigate more quantitatively the dependence of the flow response to varying terrain height, upstream static stability, and wind speed, we have conducted a variety of idealized 2D simulations. All simulations were performed with the nonhydrostatic WRF model (available online at <http://wrf-model.org>) formulated in Eulerian mass coordinates (EM core),¹ using basic dynamical and microphysical modules, with all other “physics packages” turned off. The simulations presented herein utilized the Lin et al. (1983) three-class hydrometeor scheme (i.e., rain, snow, and graupel), allowing representation of mixed warm- and cold-microphysical processes appropriate to the moist (precipitating) environments being considered. Fifth- and third-order momentum and scalar advection schemes were used in the horizontal and vertical, respectively. Calculations were made assuming both a frictionless free-slip land surface and a more realistic treatment assuming a nondimensional surface drag coefficient $C_d = 0.01$. Turbulent processes above the surface are neglected. The horizontal domain covered 400 grid points at 2-km spacing, with open lateral boundary conditions applied at the upstream and downstream ends of the domain. A stretched vertical coordinate system was used, composed of 120 layers with an approximate vertical resolution of 250 m. Rayleigh damping was implemented over the uppermost 15 km of the 30-km-deep computational domain. Model integration was carried out using a third-order Runge-Kutta scheme and time steps of 10 s.

The terrain was formulated as a 2D bell-shaped symmetric mountain with height h and half-width a placed in the center of the 800-km-wide computational domain. The geometry of the Oregon Cascades within the

IMPROVE-2 study region was approximated by a mountain height $h = 1.9$ km and half-width $a = 32$ km, while the average terrain shape of the European Alps in the Lago Maggiore region was represented by setting $h = 3.1$ km and $a = 44$ km, respectively. The results discussed here are shown windowed over a mountain-centered subset of the computational domain and after 30 h.

The atmospheric environment used to initialize the suite of idealized simulations was characterized by saturated profiles with vertically uniform moist Brunt-Väisälä frequency varying over a range of $0.03 \times 10^{-4} < N_m^2 < 1.0 \times 10^{-4} \text{ s}^{-2}$, and a temperature profile characterized by fixed surface temperature and a tropopause at 200 hPa with isothermal conditions above.² Characteristic dimensionless parameters summarizing the simulations presented here are compiled in Table 1.

All simulations neglected the Coriolis force, and this simplification can cause the flow response to a mountain barrier to extend farther upstream than observed in nature (e.g., Pierrehumbert and Wyman 1985). As our focus is on the structure of the flow over the relatively small spatial domain located directly above the steep terrain, the resulting time scales are small compared to the inertial period, leading to relatively large Rossby numbers values (between 2 and 9, see Table 1). This supports simplifying the problem by neglecting rotational effects. Certain other well-known limitations arise because of the 2D treatment of an innately 3D problem, as discussed by Doyle et al. (2000), but none of these factors substantially impact representation of cross-barrier flow over the mountain itself. Several tens of simulations were conducted to gauge the dependence of atmospheric behavior throughout a multidimensional parameter space spanned by a reasonable range of incident flow/stability conditions, terrain shape, and treatment of viscous processes. A limited subset of the simulation results obtained have been selected to highlight the essential features and sensitivity to variations of input conditions, and to further illuminate physical processes that lead to the observed structures discussed in section 4.

To explore the role of terrain in producing these flow structures, and to isolate orographic effects from other potential sources of shear (including large-scale baroclinic processes), a set of experiments was carried out in which flow toward a barrier was initialized with vertically uniform horizontal wind speed and stability. In this way, any resulting sheared flow features could be

¹ Version 1.3 of the WRF model was used. This version has been updated with several fixes to the code, as suggested by Dr. William Skamarock of NCAR.

² Except for the simulation shown in Fig. 16, whose initial conditions are described in section 5e.

TABLE 1. Rossby radius of deformation^a (L_r), Rossby number^b (Ro), Froude number^c (Fr), and relevant parameters associated with model simulations shown in section 5.

Simulation	Moist Brunt–Väisälä frequency ($N_m^2; \times 10^{-4} \text{ s}^{-2}$)	Wind speed perpendicular to terrain ($u; \text{ m s}^{-1}$)	Mountain height ($h; \times 10^3 \text{ m}$)	Mountain half-width ($a; \times 10^3 \text{ m}$)	$L_r (\times 10^3 \text{ m})$	Ro	Fr
Fig. 11a	0.03	12.5 ^d	3.1	44	54	2.84	2.33
Fig. 11b	1.00	10	3.1	44	310	2.27	0.32
Figs. 12a,b	0.03	10	3.1	44	54	2.27	1.86
Figs. 12c,d	0.30	10	3.1	44	170	2.27	0.59
Figs. 12e,f	1.00	10	3.1	44	310	2.27	0.32
Figs. 13a,b	0.03	10	1.9	32	33	3.12	3.04
Figs. 13c,d	0.30	10	1.9	32	104	3.12	0.96
Figs. 13e,f	1.00	10	1.9	32	190	3.12	0.53
Fig. 14a	0.30	20	1.9	32	104	6.25	1.92
Fig. 14b	0.30	30	1.9	32	104	9.38	2.88
Fig. 16	0.37 ^d	20 ^d	1.9	32	116	6.25	1.73

^a $L_r = (N h) f^{-1}$; f = Coriolis parameter.

^b $\text{Ro} = u (f a)^{-1}$.

^c $\text{Fr} = u (N h)^{-1}$.

^d Vertically averaged over the lowest 3 km.

directly attributed to influence by the underlying terrain. However, to better motivate this heuristic treatment, we first focus on a pair of simulations motivated by two well-documented yet markedly contrasting orographic precipitation events drawn from the MAP experiment. We close by presenting a focused examination of the best documented case from IMPROVE-2, as previously introduced in section 4b.

b. Simulation of previously documented MAP cases

To establish that the idealized model approach is reliable and sufficient for our purposes, we ran simulations including surface friction using upstream conditions corresponding to two extensively described cases from MAP, namely IOP2b and IOP8 (Bousquet and Smull 2003a,b; Medina and Houze 2003; Rotunno and Ferretti 2003; Steiner et al. 2003). These two cases were canonical in the sense that they differed markedly in the way that the flow and precipitation responded to the Alpine mountain barrier. As such, they serve as a desirably stringent test of the model's ability to represent orographic processes over a range of physically plausible conditions.

IOP2b was characterized by a nearly neutral to slightly unstable upstream flow and wind component normal to the barrier exhibiting a low-level jet (Figs. 8b and 9b, respectively, of Medina and Houze 2003). In the corresponding idealized simulation, upstream conditions were specified using a simplified wind profile [viz. a uniform 10 m s^{-1} wind and superposed a 2-km-deep jet exhibiting peak speeds of 20 m s^{-1} centered at 1 km MSL with linear shear above/below the jet core,

and vertically uniform nearly-neutral stable stratification ($N_m^2 = 0.03 \times 10^{-4} \text{ s}^{-2}$)]³. In the simulation of IOP2b, the low-level jet maintained coherency as it rose over the windward terrain slopes (Fig. 11a). The simulated steady state cross-barrier field over the windward slope of the terrain in Fig. 11a is highly consistent with the observed time-mean Doppler radial velocity pattern for IOP2b (cf. Fig. 12b of Medina and Houze 2003). Simulated flow in the lee of the Alpine-like barrier (i.e., near the rightmost edge of Fig. 11a) includes enhanced downslope winds that exhibit some aspects of mountain wave behavior. No corresponding detailed observations exist with which to verify this feature.

By contrast, the IOP8 case had a profoundly stable low-level flow with a moist Brunt–Väisälä frequency ~ 30 times that in IOP2b (see Table 1). The simulation results in Fig. 11b use for initialization vertically uniform values of horizontal wind speed (10 m s^{-1}) and stability ($N_m^2 = 1.0 \times 10^{-4} \text{ s}^{-2}$) obtained by averaging the lowest 3 km of the upstream sounding. The contours of the wind normal to the barrier in the simulation show strong flow retardation and reversal over the windward slopes at the lower levels. The isotachs above the 3-km level bend downward toward the crest of the terrain, indicating a further deceleration (upstream blocking) of the wind as the airstream approached the Alps. This structure is again highly consistent with the observed Doppler radial velocity field for IOP8 (cf. Fig. 7). Strong downslope flow in the lee of the Alps con-

³ Use of a nearly neutral, yet slightly stable stratification avoided the undesirable complication of convective overturning.

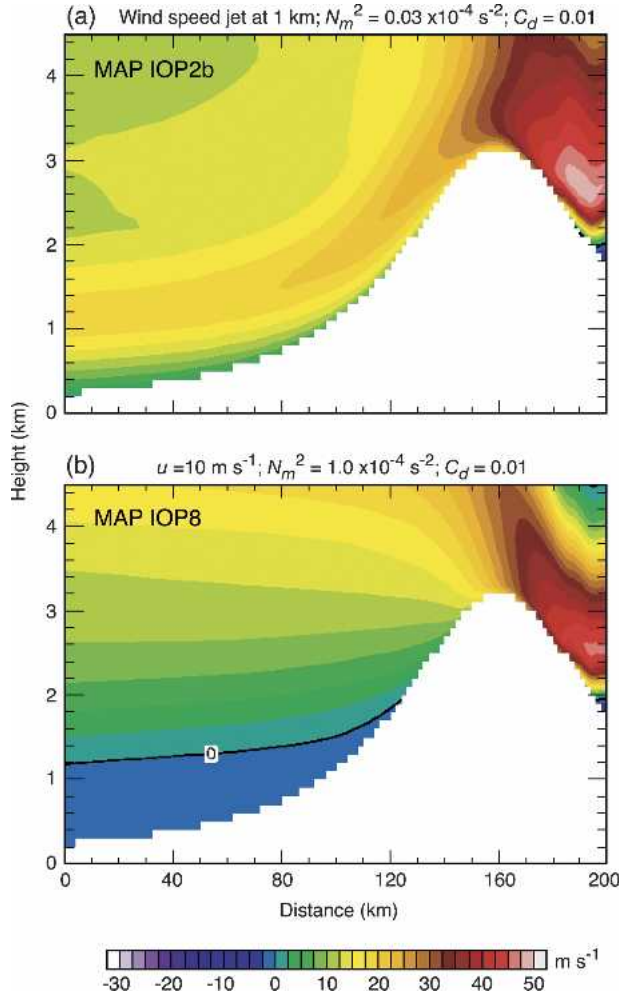


FIG. 11. Vertical cross section of simulated moist flow past a 2D bell-shaped mountain with height of 3.1 km and half-width of 44 km (representing the European Alps), as revealed after 30 h of integration using the WRF model with Lin et al. (1983) microphysics. Horizontal wind speed is shown in color, with positive values denoting flow from left to right and 0 m s^{-1} indicated by the black contour. Horizontal distance is label from the left edge of the display domain, which is a subset of the computational domain (see text). (a) Model run initialized with a saturated sounding having surface temperature $T_s = 293 \text{ K}$ and vertically uniform static stability ($N_m^2 = 0.03 \times 10^{-4} \text{ s}^{-2}$). The wind speed profile was vertically uniform (10 m s^{-1}) everywhere except for a layer between the surface and 2 km, where speeds increased linearly to reach a peak value of 20 m s^{-1} at an altitude of 1 km. (b) Model run initialized with a saturated sounding with surface temperature $T_s = 283 \text{ K}$, vertically uniform static stability ($N_m^2 = 1.0 \times 10^{-4} \text{ s}^{-2}$) and wind speed (10 m s^{-1}). Both runs were obtained using surface nondimensional drag coefficient $C_d = 0.01$.

forms to the notion of a rearward-tilted wave response to the barrier.

The many similarities between the simulated patterns depicted in Figs. 11a,b and extensive Doppler radar observations obtained during MAP IOP2b and IOP8

argue strongly that the model is capturing the orographically modified flow in a sufficiently realistic way to merit its further use as a tool for exploring the origin of the cross-barrier flow features seen in section 4.

c. Stability experiments

In this study, we seek to determine if the wind fields observed by Doppler radar in the stable upstream flow cases of MAP and IMPROVE-2 are a characteristic response of the upstream flow to terrain forcing (as opposed to, for example, simply being some inherent property of the parent baroclinic storm system). We therefore begin with a series of experiments initialized with vertically uniform wind speed. The atmospheric environment used to initialize these idealized simulations was characterized by saturated profiles with vertically uniform moist Brunt–Väisälä frequency varying over a range of $0.03 \times 10^{-4} < N_m^2 < 1.0 \times 10^{-4} \text{ s}^{-2}$, vertically uniform horizontal wind speeds of 10 m s^{-1} , and a fixed surface temperature of $T_s = 283 \text{ K}$. The varying degrees of upstream moist static stability assumed yield a range of Froude number values (between 0.3 and 3, see Table 1) and associated dynamical behavior. Figure 12 shows the horizontal wind speed (color shading) and vertical wind shear (contours) for a suite of simulations conducted using an Alpine-like barrier. Figures 12a,c,e show results for free-slip conditions. Thus the flow variations depicted in these simulations are entirely due to the presence of the mountain. Moist and nearly neutral conditions ($N_m^2 = 0.03 \times 10^{-4} \text{ s}^{-2}$)—often seen in conjunction with orographic precipitation events, as discussed by Miglietta and Rotunno (2005) and the references therein—enable the simulated flow to easily surmount the Alpine barrier (Fig. 12a). With increasing atmospheric stability, the free-slip flow below crest height progressively slows down on the windward side of the barrier, and the vertical shear over the windward slope increases (Figs. 12c,e). The experiment based upon the most stable upstream profile exhibits an elevated layer of vertical shear that tilts upward over the windward slope, beneath which there develops a deep layer of profoundly blocked low-level flow (viz. negative flow speed values below 1 km in Fig. 12e). This simulated behavior is reminiscent of observed conditions during MAP IOP8, which included fully reversed (downslope) low-level flow, as was previously discussed in section 5b. By contrast, under moist-neutral conditions (Fig. 12a), flow speeds increase monotonically toward the crest (as required by mass flux conservation in a Bernoulli-like sense), but exhibit comparatively little vertical shear (Fig. 12a). In the presence of increasingly stable stratification, the upstream flow above crest level is signifi-

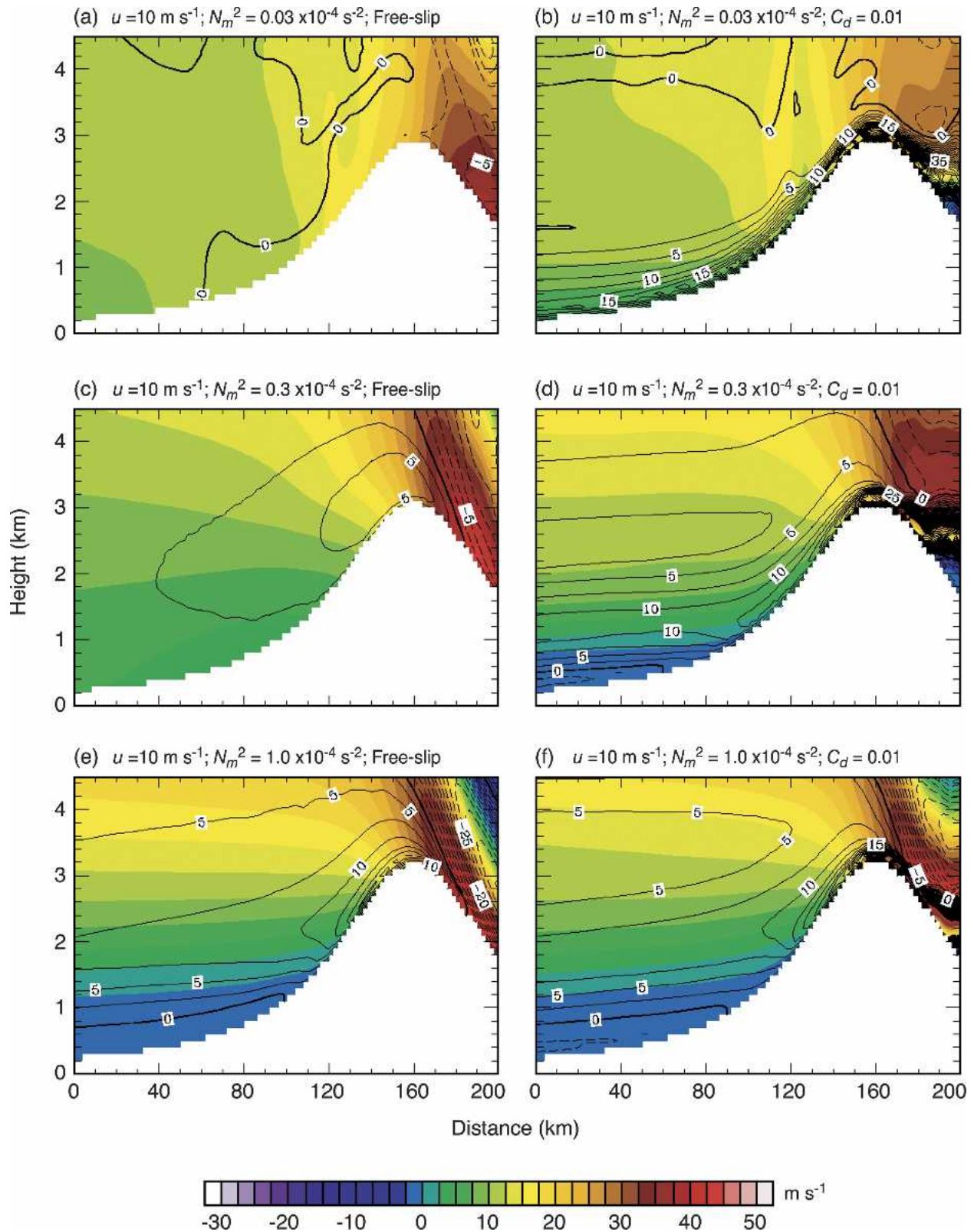


FIG. 12. As in Fig. 11b, but assuming static stability values: (a), (b) $N_m^2 = 0.03 \times 10^{-4} \text{ s}^{-2}$; (c), (d) $N_m^2 = 0.3 \times 10^{-4} \text{ s}^{-2}$; and (e), (f) $N_m^2 = 1.0 \times 10^{-4} \text{ s}^{-2}$. Horizontal wind speed is shown in color, while the vertical shear (du/dz , where z is the vertical coordinate) is shown by black contours at $2.5 \text{ m s}^{-1} \text{ km}^{-1}$ intervals. (left) Model runs assumed a frictionless land surface. (right) model runs obtained using surface nondimensional drag coefficient $C_d = 0.01$.

cantly accelerated relative to the 10 m s^{-1} value imposed at the model's lateral boundary (Figs. 12c,e), and terrain effects induce progressively greater amounts of shear in the upstream subcrest layer. The shear layer near the 2-km level over the lower windward slope appears most prominently when the stability is maximized (Fig. 12e). Houze and Medina (2005) emphasized the low-level shear layer appearing in stable flow approaching the barrier may set up turbulence, which in turn aids precipitation growth over the lower windward slope of the barrier. The experiments in Figs. 12a,c,e show that this shear layer, which ultimately helps enhance the precipitation, can emerge as a response of the flow to the terrain even in the absence of surface friction under stable conditions. In actual orographically modified flows, this mechanism allows turbulent overturning to aid precipitation growth over the windward slope in the absence of buoyant instability.

For obvious reasons, the choice of free-slip lower boundary conditions may not render realistic near-surface flow over mountainous terrain. Therefore, additional simulations were carried out that incorporated friction at the land surface to test sensitivity of these results to treatment of the lower boundary. These results are shown in Figs. 12b,d,f. The effect of surface friction is to substantially increase the near-surface shear on both the windward and leeward sides of a barrier, particularly in the presence of less stably stratified flow (for which generally stronger low-level momentum is subject to dissipation). Friction thus causes the upstream low-level flow to decelerate even further, yielding a more pronounced shear layer that virtually blankets the windward mountain slopes under moist nearly neutral conditions (cf. Figs. 12a,b). In fact, this friction-induced deceleration is substantial enough to induce a reverse (downslope) flow under intermediate stability conditions (cf. Figs. 12c,d). For the most stable simulation, the effect of friction on the windward slope is slight (cf. Figs. 12e,f). In the lee of the barrier, inclusion of surface friction effectively reduces the simulated flow's sensitivity to varying atmospheric stability, as the upper reaches of the lee slopes in Figs. 12b,d,f are more uniformly characterized by a thin (approximately 500 m thick) surface-based layer of strong vertical shear that is ultimately shed by the mountain in the downstream direction.

Figure 13 contains an analogous set of simulation results employing underlying terrain whose foreshortened vertical and horizontal scales are more representative of the Oregon Cascades apropos to our observations during IMPROVE-2. Simulations with a free-slip lower boundary show that increased upstream stability again results in the production of progressively greater

vertical shear over the windward slopes, with the intensity and upstream extension of this mountain-induced shear and accompanying downstream gravity wave behavior all markedly increasing under conditions of greater stability (Figs. 13a,c,e). The inclusion of friction at the lower boundary increases the near-surface shear (Figs. 13b,d,f), which is again more marked for simulations characterized by weak stability (Figs. 13a,b). The IMPROVE-2 case described in section 4b (section 4c) exhibited low-level mean stability of $N_m^2 = 0.37 \times 10^{-4} \text{ s}^{-2}$ ($0.57 \times 10^{-4} \text{ s}^{-2}$) (see Fig. 5) and low-level mean wind speed of 20 m s^{-1} (23 m s^{-1}), which corresponds to a Froude number (Fr) of 1.7 (1.6). This is an intermediate state between that represented by Figs. 13a,b (Fr = 3) and Figs. 13c,d (Fr = 1) (Table 1). In this Fr regime, the shear layer does not convincingly appear in the absence of friction (Figs. 13a,c). Surface friction does, however, lead to a slightly elevated layer of maximum shear, particularly in situations of intermediate stability (Fig. 13d). Although the idealized simulation summarized in Fig. 13e suggests that a robust shear layer could develop over a Cascade-like barrier as a result of stability alone, such strong stratification was not observed in the IMPROVE-2 cases. Thus, the flow over the Cascades appears to differ from that over the Alps, where large stability and terrain-flow interactions alone may be sufficient to produce strong shear. In the Cascades case, the shear layer is apparently produced primarily by friction with the stability playing a lesser role.

Addition of surface friction causes a low-level flow deceleration on the windward side in both the Alps and Cascades cases. In the presence of otherwise identical upstream conditions, low-level flow reversal is, however, less prone to occur upstream of the smaller barrier (cf. Figs. 12d and 13d), in full agreement with well-known energetic principles (Smith 1979).

d. Upstream wind speed experiments

The response of the flow to the presence of the mountain barrier depends on stability, wind speed, shear, and the height of the barrier. The experiments described above were conducted by varying the stability for two different mountain barrier heights (Alps and Cascades). To examine the corresponding role of the upstream wind speed, we adopt a constant stability (as represented in Fig. 13d) and now vary incident flow to similarly span a range of Froude number behavior. In these simulations $N_m^2 = 0.30 \times 10^{-4} \text{ s}^{-2}$, and surface friction is included. Figure 14a (Fig. 14b) presents results from a simulation in which the incident flow speed was 20 m s^{-1} (30 m s^{-1}), yielding Fr = 2 (Fr = 3; see

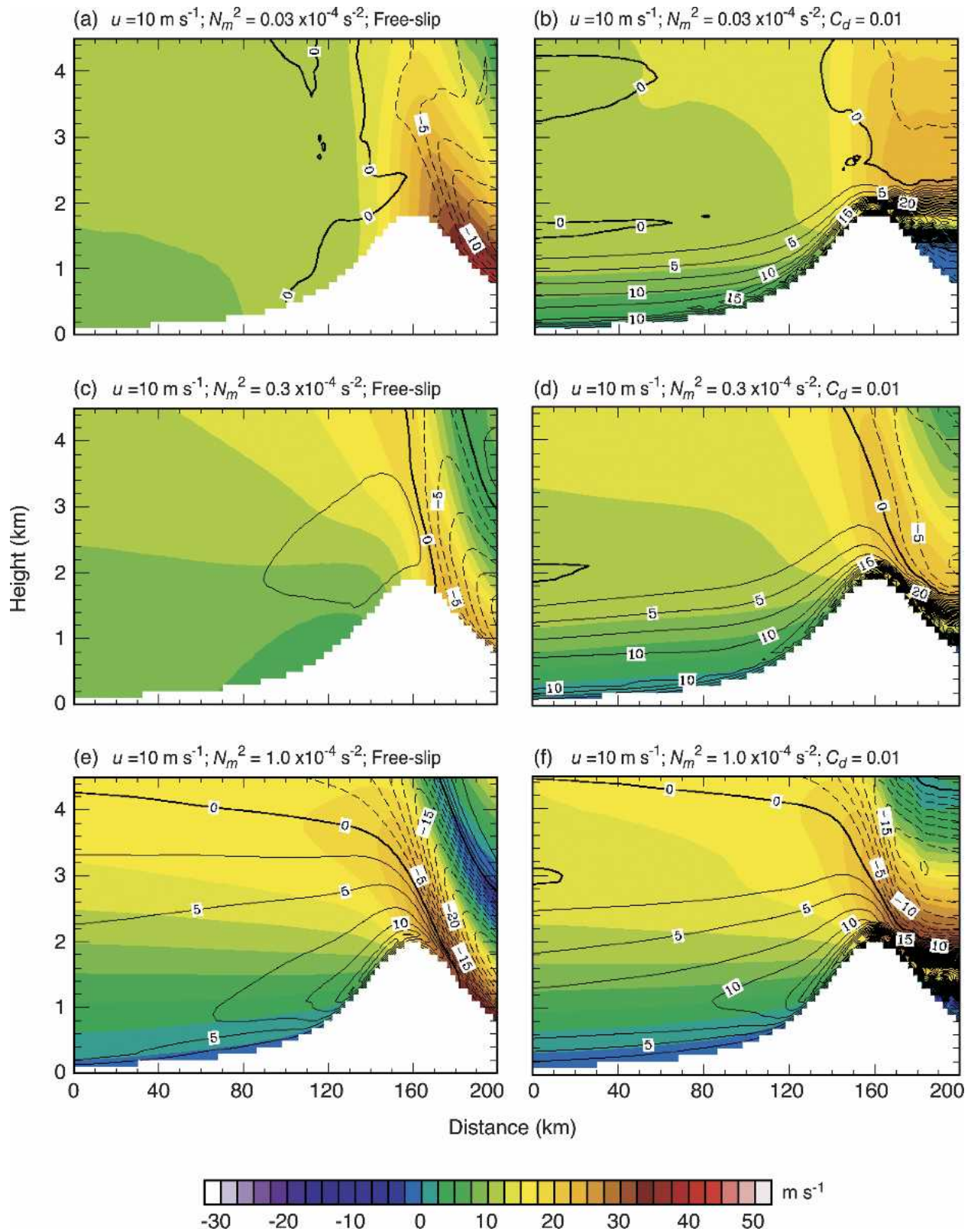


FIG. 13. As in Fig. 12, but using a 2D bell-shaped mountain with height of 1.9 km and half-width of 32 km (representing the Cascades).

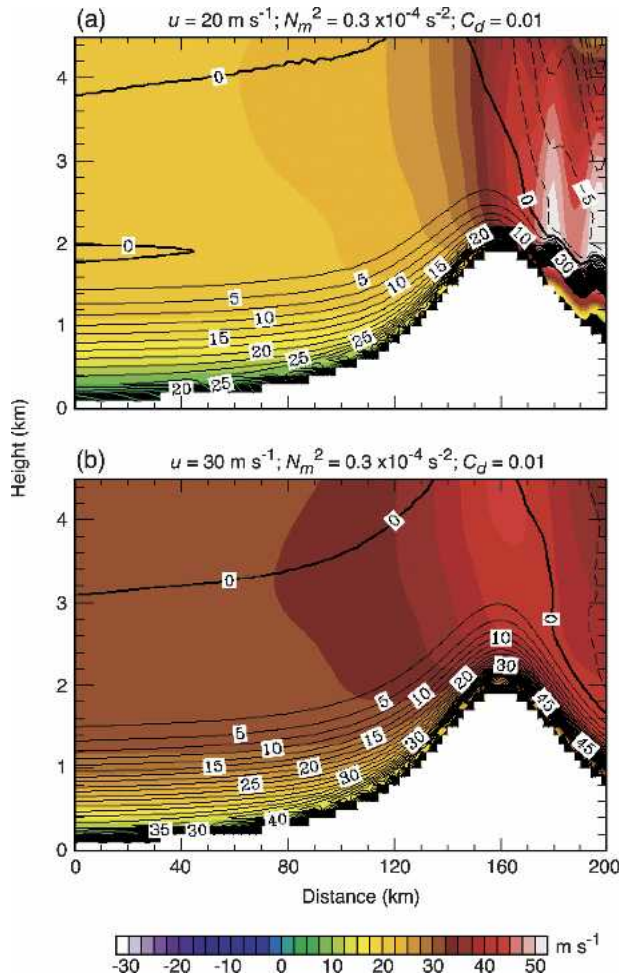


FIG. 14. As in Fig. 13, but initialized with a saturated sounding with vertically uniform static stability ($N_m^2 = 0.3 \times 10^{-4} \text{ s}^{-2}$), and vertically uniform wind speed of (a) $u = 20 \text{ m s}^{-1}$ and (b) $u = 30 \text{ m s}^{-1}$.

Table 1). In terms of similarity theory, these results are comparable to those shown in Figs. 12b and 13b.

e. Simulation of the 13–14 December 2001 IMPROVE-2 case

The idealized simulations described above provide a useful context in which to interpret the observations obtained in the comprehensively observed 13–14 December 2001 IMPROVE-2 storm (Figs. 8 and 9). We have devised a corresponding, more realistic simulation using upstream wind and stability profiles that are based on the observations and are not vertically uniform. We use a simplified version of an upstream sounding (UW in Fig. 1b) released at 2356 UTC on 13 December 2001 (Fig. 15, solid line). As with the previously discussed simulations, this sounding was applied

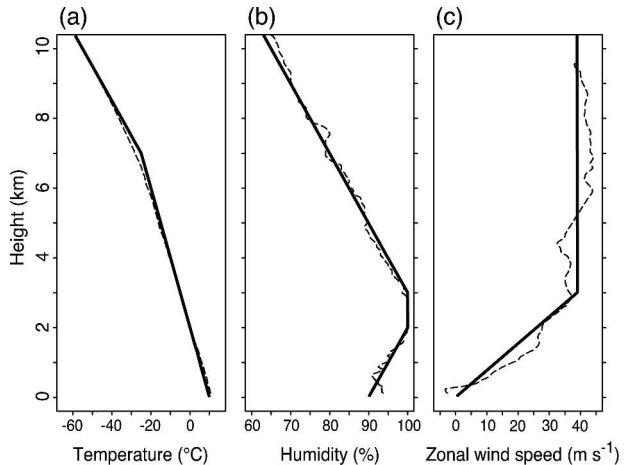


FIG. 15. Sounding released at 2356 UTC 13 Dec 2001 over the Willamette Valley (UW in Fig. 1b). Dashed lines indicate observed quantities, while solid lines depict simplified profiles used to initialize the idealized simulation shown in Fig. 16.

at the upstream lateral boundary of the model domain (i.e., at a distance of 400 km from the mountain crest). Surface friction was included, and the results are shown at 30 h into the integration, by which time the flow had reached steady state.

The structure of the simulated cross-barrier flow (Fig. 16) is highly reminiscent of that depicted in the observations (Fig. 9b). The simulation thus captures the essential processes producing the shear layer. The isotachs in Fig. 16a bend up over the windward slope as in Fig. 9b, and embody flow retardation at low levels. A thin near-surface layer of reversed flow appears, but the preponderance of the incident cross-barrier airstream ultimately surmounts the barrier (albeit after passing through the windward zone of flow deceleration and lifting). The flow contours reach peak heights (denoting maximum flow deceleration at any given level) near the crest (Fig. 16a). Immediately downstream of the crest, the contours of the airflow crossing the barrier plummeted, denoting strong momentum transport toward the surface. This pattern is consistent with mountain-induced gravity wave behavior, which has been the subject of many previous simulations focusing on the leeside flow behavior (e.g., Durran and Klemp 1983). Figure 16b shows that the flow response formed a slightly elevated layer of enhanced shear exceeding $17.5 \text{ m s}^{-1} \text{ km}^{-1}$ (representing an $\sim 5 \text{ m s}^{-1} \text{ km}^{-1}$ enhancement over the initial upstream conditions) that tilts upward over the windward slopes and extends up and over the crest. A secondary layer of weak shear appearing near 3-km altitude is the result of an artificially sharp transition from gradually increasing wind speeds below to constant winds above that level,

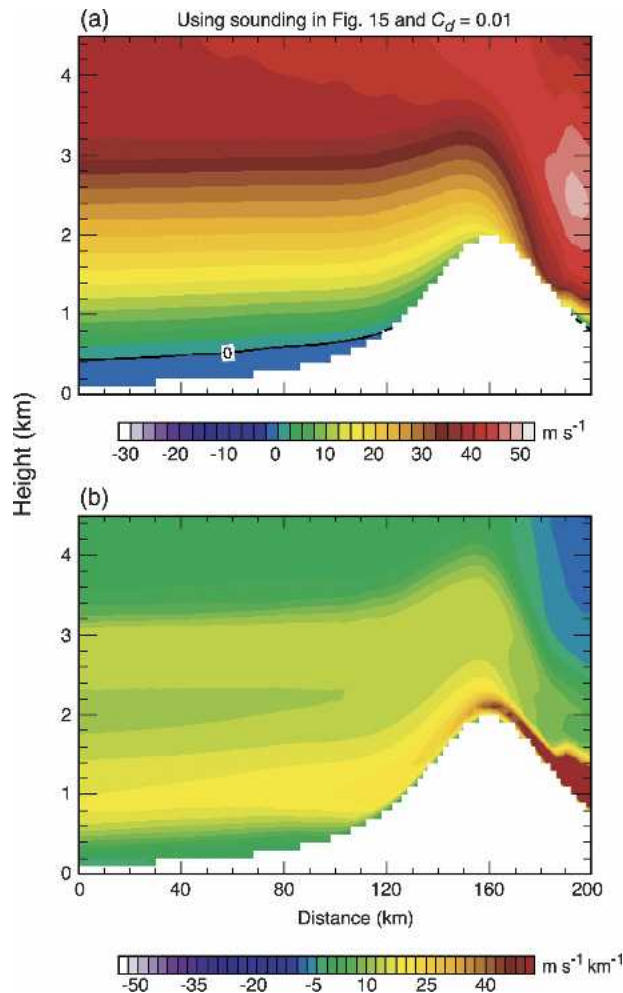


FIG. 16. As in Fig. 14, but initialized using a simplified version of a sounding obtained during the 13–14 Dec 2001 IMPROVE-2 case (as shown in Fig. 15). (a) Horizontal wind speed, with 0 m s^{-1} indicated by the black contour, (b) vertical wind shear.

as introduced by the idealized sounding (Fig. 15c). The low-level shear layer is the feature emphasized by Houze and Medina (2005) as providing a mechanism for turbulent overturning and associated precipitation particle growth over the windward slope. These calculations show that this shear layer is an inherent feature of the flow over the mountainous terrain. While moderate stability contributes somewhat to the development of the shear layer, the contribution of friction and vertical gradients in the upstream wind profile (as embodied in Fig. 15c) are fundamental to this characteristic flow pattern.

6. Conclusions

Baroclinic systems approaching the European Alps and the Oregon Cascades in situations of stable up-

stream stratification exhibit similar cross-barrier flow and precipitation features on the windward side of the mountain ranges. Blocked or partially retarded flow develops at low levels, with a shift to more strongly cross-barrier flow above. A layer of strong vertical wind shear forms at intermediate heights in the subcrest layer. This shear layer generally slopes upward toward the mountain crest, with evidence of local undulations over prominent foothill peaks. The present study shows this shear layer to be a persistent and characteristic feature of midlatitude baroclinic storms passing over a mountain range. The observed repeatability of this shear layer from case to case and region to region and its persistence within individual cases suggest that it is an essential component of the orographic precipitation process over certain regions, such as the Alps and the Cascades.

When the shear layer is present, the precipitation over the windward slope exhibits a stratiform structure, and is marked by a prominent radar bright band. These highly sheared events are further characterized by a midlevel secondary maximum of reflectivity over and immediately upstream of the crest, whose development is apparently connected to the lifting that spans the barrier in association with a tilted, upward-propagating gravity wave disturbance. Airborne radar data extending leeward of the crest line indicate that strong down-slope winds (though not always extending fully to the surface) are a characteristic element of this standing, terrain-induced gravity wave flow.

Idealized numerical simulations of flow over a 2D bell-shaped mountain, performed using the Weather Research and Forecasting (WRF) model, provide insight into the origins of the ubiquitous shear layer identified in this study. These simulations indicate that, in the presence of sufficient upstream static stability, orographic effects alone are sufficient to support the development of the upward-sloping shear layer on the windward side of the mountain range. Sensitivity tests indicate that flow retardation and vertical shear strength increase with increasing stability. In agreement with theory, moist simulations suggest that flow retardation (and even blocking and associated flow reversal) is accentuated when the mountain height is increased. Surface friction and/or preexisting (e.g., baroclinically induced) vertical shear also serve to enhance the strength of the orographic shear layer that envelops the region of prominent terrain. In the extremely stable case of MAP IOP8, formation of the characteristic shear layer is explained almost entirely by the stability of the flow, as numerical experiments demonstrate the shear layer to be almost exclusively the result of the stable flow rearranging itself as it impinges upon the

Alpine barrier. In the IMPROVE-2 cases, which embody less profoundly stable flow approaching mountains of more modest stature, the impacts of surface friction and/or preexisting low-level shear appear to be primary contributing factors, with stability playing a secondary role in forming the shear layer over the windward slopes of the Cascade Range.

The pervasive presence of enhanced low-level shear described in this paper in the heavy precipitation zones of midlatitude frontal systems passing over mountain ranges suggests a fundamental dynamical–microphysical interaction leading to the local enhancement of the frontal precipitation over the windward slopes of major mountain ranges. Model simulations indicate that this shear layer is part of the natural response of a stable flow encountering a mountain barrier. The parts of the storm that are stable, laden with moisture and accompanied by a strong cross-barrier flow component above the lowest levels will develop this characteristic shear pattern, as a consequence of the stability of the flow and frictional drag over the underlying surface. This layer can develop in the presence of unsheared (i.e., vertically uniform) upstream flow, but is enhanced if the upstream wind profile possesses preexisting low-level shear. The shear layer formed by these orographically induced dynamical processes in turn favors turbulent overturning within the airstream passing over the mountain range, and this turbulence in turn promotes the growth of precipitation-sized particles and hence concentration (via more rapid fallout) of precipitation over the windward slopes (Houze and Medina 2005). Thus, even a stable extratropical cyclone passing over a sufficiently tall mountain has the dynamical capacity to establish a flow regime that effectively favors orographic enhancement of precipitation over the windward slopes.

Acknowledgments. Professor Cliff Mass and two anonymous reviewers made detailed and insightful comments. Amy Haase, Stacy Brodzik, Janae Nash, and Sean Casey contributed to the data processing. Beth Tully and Kay Dewar edited the figures. Drs. Jimmy Dudhia and William Skamarock of the National Center for Atmospheric Research (NCAR) provided valuable guidance for the WRF simulations. This research was sponsored by the National Science Foundation (NSF) under Grant ATM-0221843 to the University of Washington. The numerical simulations were supported by NSF Grant ATM-0223798 to Princeton University.

REFERENCES

- Bougeault, P., and Coauthors, 2001: The MAP Special Observing Period. *Bull. Amer. Meteor. Soc.*, **82**, 433–462.
- Bousquet, O., and B. F. Smull, 2003a: Airflow and precipitation fields within deep alpine valleys observed by airborne Doppler radar. *J. Appl. Meteor.*, **42**, 1497–1513.
- , and —, 2003b: Observations and impacts of upstream blocking during a widespread orographic precipitation event. *Quart. J. Roy. Meteor. Soc.*, **129**, 391–409.
- Colle, B. A., 2004: Sensitivity of orographic precipitation to changing ambient conditions and terrain geometries: An idealized modeling perspective. *J. Atmos. Sci.*, **61**, 588–606.
- , and C. F. Mass, 1996: An observational and modeling study of the interaction of low-level southwesterly flow with the Olympic Mountains during COAST IOP 4. *Mon. Wea. Rev.*, **124**, 2152–2175.
- Cox, J. A. W., W. J. Steenburgh, and D. E. Kingsmill, 2002: Dual-Doppler analysis of the kinematic structure of a Wasatch Mountain winter storm. Preprints, *10th Conf. on Mountain Meteorology*, Park City, UT, Amer. Meteor. Soc., 139–140.
- Doyle, J. D., and Coauthors, 2000: An intercomparison of model-predicted wave breaking for the 11 January 1972 Boulder windstorm. *Mon. Wea. Rev.*, **128**, 901–914.
- Durrán, D. R., and J. B. Klemp, 1982: On the effect of moisture on Brunt–Väisälä frequency. *J. Atmos. Sci.*, **39**, 2152–2158.
- , and —, 1983: A compressible model for the simulation of moist mountain waves. *Mon. Wea. Rev.*, **111**, 2341–2363.
- Garvert, M. F., B. A. Colle, and C. F. Mass, 2005: The 13–14 December 2001 IMPROVE-2 event. Part I: Synoptic and mesoscale evolution and comparison with a mesoscale model simulation. *J. Atmos. Sci.*, **62**, 3474–3492.
- Houze, R. A., Jr., and S. Medina, 2005: Turbulence as a mechanism for orographic precipitation enhancement. *J. Atmos. Sci.*, **62**, 3599–3523.
- Jiang, Q., 2003: Moist dynamics and orographic precipitation. *Tellus*, **55A**, 301–316.
- Lin, Y.-L., R. D. Farley, and H. D. Orville, 1983: Bulk parameterization of the snow field in a cloud model. *J. Climate Appl. Meteor.*, **22**, 1065–1092.
- Marwitz, J. D., 1983: The kinematics of orographic airflow during Sierra storms. *J. Atmos. Sci.*, **40**, 1218–1227.
- , 1987: Deep orographic storms over the Sierra Nevada. Part I: Thermodynamic and kinematic structure. *J. Atmos. Sci.*, **44**, 159–173.
- Mass, C. F., and G. K. Ferber, 1990: Surface pressure perturbations produced by an isolated mesoscale topographic barrier. Part I: General characteristics and dynamics. *Mon. Wea. Rev.*, **118**, 2579–2596.
- Medina, S., and R. A. Houze Jr., 2003: Air motions and precipitation growth in alpine storms. *Quart. J. Roy. Meteor. Soc.*, **129**, 345–371.
- Meyers, M. P., and W. R. Cotton, 1992: Evaluation of the potential for wintertime qualitative precipitation forecasting over mountainous terrain with an explicit cloud model. Part I: Two-dimensional sensitivity experiments. *J. Appl. Meteor.*, **31**, 26–50.
- Michalakes, J., S. Chen, J. Dudhia, L. Hart, J. Klemp, J. Middlecoff, and W. Skamarock, 2001: Development of a next-generation regional weather research and forecasting model. *Developments in Teracomputing: Proceedings of the 9th ECMWF Workshop on the Use of High Performance Computing in Meteorology*, W. Zwiefelhofer and N. Kreitz, Eds., World Scientific, 269–276.

- Miglietta, M. M., and R. Rotunno, 2005: Simulations of moist nearly neutral flow over a ridge. *J. Atmos. Sci.*, **62**, 1410–1427.
- National Climatic Data Center, 2001: *Storm Data*. Vol. 43, No. 12, 106 pp.
- Pierrehumbert, R. T., and B. Wyman, 1985: Upstream effect of mesoscale mountains. *J. Atmos. Sci.*, **42**, 977–1003.
- Rotunno, R., and R. Ferretti, 2003: Orographic effects on rainfall in MAP Cases IOP 2b and IOP 8. *Quart. J. Roy. Meteor. Soc.*, **129**, 373–390.
- Skamarock, W. C., J. B. Klemp, and J. Dudhia, 2001: Prototypes for the WRF (Weather Research and Forecasting) model. Preprints, *Ninth Conf. on Mesoscale Processes*, Fort Lauderdale, FL, Amer. Meteor. Soc., J11–J15.
- Smith, R. B., 1979: The influence of mountains on the atmosphere. *Advances in Geophysics*, Academic Press, Vol. 21, 87–230.
- Steiner, M., O. Bousquet, R. A. Houze, B. F. Smull, and M. Mancini, 2003: Airflow within major alpine river valleys under heavy rainfall. *Quart. J. Roy. Meteor. Soc.*, **129**, 411–431.
- Stoelinga, M. T., and Coauthors, 2003: Improvement of Microphysical Parameterization through Observational Verification Experiment. *Bull. Amer. Meteor. Soc.*, **84**, 1807–1826.
- Woods, C. P., M. T. Stoelinga, J. D. Locatelli, and P. V. Hobbs, 2005: Microphysical processes and synergistic interaction between frontal and orographic forcing of precipitation during the 13 December 2001 IMPROVE-2 event over the Oregon Cascades. *J. Atmos. Sci.*, **62**, 3493–3579.